A temporal fourth-order scheme for the first-order acoustic wave equations

Guihua Long,[1,2,3] Yubo Zhao[1] and Jun Zou[4]

[1]*Shenzhen Institutes of Advanced Technology, Chinese Academy of Sciences, Shenzhen 518055, China. E-mail: gh.long@siat.ac.cn*
[2]*Technological Research Center of Shenzhen Municipal Engineering Corporation, Shenzhen 518034, China*
[3]*Department of Earth Sciences, Zhejiang University, Hangzhou 310027, China*
[4]*Department of Mathematics, The Chinese University of Hong Kong, Shatin, Hong Kong*

SUMMARY

In this paper, we propose a temporal fourth-order scheme for solving the 2-D first-order acoustic wave equations with perfectly matched layers in time domain. For the temporal discretization, we approximate the velocity at mid-points and the pressure at grid points, then expand the velocity and pressure by Taylor series and replace the high-order temporal derivatives by spatial derivatives. For the spatial discretization, we apply the Fourier pseudospectral method based on conventional and staggered-grid schemes. The dispersion and stability of the new scheme are analysed, and numerical simulations are presented to confirm the robustness and efficiency of the scheme. The new scheme is eventually applied for the wavefield modelling and reverse time migration in bilayered and heterogeneous media to further verify its accuracy and efficiency.

Key words: Numerical solutions; Fourier analysis; Wave propagation.

1 INTRODUCTION

The delineation of Earth's structures from seismic data, which are usually obtained by waveform inversion or migration, requires accurate and efficient numerical methods for computing synthetic seismograms. The methods that have been widely used in seismic modelling include finite difference methods (FDMs, e.g. Virieux 1986; Levander 1988; Igel *et al.* 1995; Moczo *et al.* 2000; Tessmer 2000), pseudospectral methods (PSMs, e.g. Gazdag 1981; Kosloff & Baysal 1982; Fornberg 1988; Takenaka *et al.* 1999), finite element methods (FEMs, e.g. Ciarlet 1991; Yoshimura *et al.* 2003; Moczo *et al.* 2011), spectral element methods (SEMs, Komatitsch & Vilotte 1998; Komatitsch & Tromp 2002; Chaljub *et al.* 2007; Moczo *et al.* 2011), etc. For a more detailed understanding of the recent development of these methods, we refer to the survey articles by Moczo *et al.* (2007a,b, 2011).

Most aforementioned methods have their own merits and drawbacks in either efficiency or accuracy. Classical schemes such as low-order FDMs and FEMs suffer from numerical dispersion or errors, which can be improved, by either refining spatial grids or constructing methods with higher orders of accuracy (Dablain 1986; Fornberg 1988; Käser & Dumbser 2006; Dumbser *et al* 2007; Käser & de la Puente 2008; Liu & Sen 2009a). For an application problem, one may have a more detailed analysis on the dispersion relation or discretization error of a scheme, then improve its accuracy and efficiency by some optimization techniques (e.g. Holberg 1987; Geller & Takeuchi 1998; Moczo *et al.* 2002; Yang *et al.* 2003; Galis *et al.* 2008; Liu & Sen 2009a).

When spatial grids are refined while time steps are fixed, the number of grid points is increased per wavelength, hence the numerical dispersion of the concerned scheme can be improved, but it may cause the instability of the scheme. Because of the dominance of the spatial accuracy, one can not improve the accuracy of a numerical method essentially by reducing time steps or improving temporal accuracies while spatial grids are fixed. As higher-order temporal schemes are more demanding in terms of computational efforts and storage (Liu & Sen 2009b), second-order central difference scheme for time marching is usually preferred when high-order spatial schemes are used. However, it has also positive effects to improve temporal accuracies, for instance, it can relax the CFL condition and improve the dispersion relation (Chen 2009), which are two of the key ingredients for a numerical method.

There are many other effective methods for suppressing dispersion and numerical errors, such as the optimized FDM (e.g. Geller & Takeuchi 1998) and the nearly analytic discrete method (NADM, Yang *et al.* 2003). Unlike the usual high-order schemes, these two methods use some optimized operators or nearly analytic derivative formulations for temporal or spatial discretizations to improve numerical accuracies. Other methods include the ones that are based on expansion techniques (Kosloff *et al.* 1989; Chen 2007; Soubaras & Zhang 2008; Zhang & Zhang 2009; Pestana & Stoffa 2010). For example, the second-order temporal Lax-Wendroff scheme was developed by using

Taylor expansion. One can further develop higher-order temporal schemes by replacing high-order temporal derivatives by spatial derivatives (Dablain 1986; Chen 2007). Another expansion method is the two-step explicit marching scheme, which extrapolates the wavefield by using the pseudo-differential technique that shifts implicitly high-order temporal derivatives to spatial ones (Soubaras 1996; Soubaras & Zhang 2008). This two-step method is highly accurate for homogeneous media, but it encounters difficulties in approximating the pseudo-differential operator involved when large velocity contrasts are present. Alternatively, the rapid expansion method proposed by Kosloff *et al.* (1989) can be used to obtain a more accurate time integration for the second-order wave equation. Similarly to Tal-Ezer *et al.* (1987), Bessel functions and modified Chebyshev polynomials are incorporated in the method to expand the involved *cosine* operator so that it is highly accurate and numerically stable with large time steps.

All the aforementioned high-order methods, except for the Lax-Wendroff scheme, have been applied for reverse time migration (RTM), but most of them are constructed for the second-order acoustic wave equation. Compared with the second-order equation, the first-order acoustic wave system has a superior property for incorporating perfectly matched layers (PML) boundary conditions (Berenger 1994; Chew & Liu 1996; Collino & Tsogka 2001; Komatitsch & Martin 2007; Kristek *et al.* 2009). Although some PML boundary conditions were developed for the second-order wave equation (Komatitsch & Tromp 2003), high-order temporal derivatives are involved in their PML equations under the stretched coordinates, hence numerical treatments are usually rather technical and complicated. Another PML method, which was developed in Grote & Sim (2010), is able to keep temporal derivatives only up to second order, but it introduces several auxiliary variables, which are non-physical and increase computational complexity greatly. On the contrary, many simple and effective PML boundary conditions have been developed for the first-order acoustic wave equations (Sacks *et al.* 1995; Drossaert & Giannopoulos 2007), which will be the major focus of this work.

In this work, we propose a temporal fourth-order scheme for effectively solving the first-order acoustic wave equations. For the temporal discretization, we approximate the velocity at mid-points and the pressure at grid points, then expand the velocity and pressure by Taylor series and replace the high-order temporal derivatives by spatial derivatives. For the spatial discretization, we apply the PSM formulated on conventional and staggered grids. The PSM provides optimal spatial accuracy for a given grid size and its realization by fast Fourier transform (FFT) leads to high computational efficiency (Kosloff & Baysal 1982; Fornberg 1988). To absorb spurious reflections caused by artificial boundaries, we incorporate the split PML technique in our numerical scheme. The dispersion and stability of this new scheme are analysed, and the scheme is eventually applied for wavefield modelling and RTM in bilayered and heterogeneous media.

2 FIRST-ORDER ACOUSTIC WAVE EQUATIONS WITH TEMPORAL DISCRETIZATION

The acoustic wave propagating in a heterogeneous medium can be described by

$$\rho \nabla \cdot \left(\frac{1}{\rho} \nabla p \right) - \frac{1}{v^2} \frac{\partial^2 p}{\partial t^2} = -\rho \frac{\partial^2 i_V}{\partial t^2}, \tag{1}$$

where p and i_V are, respectively, the acoustic pressure and a point source of volume injection (e.g. airguns), and $v = \sqrt{\kappa/\rho}$ is the velocity of wave propagating in the medium, with ρ being the density and κ the adiabatic compression modulus.

By introducing a vector $\mathbf{v}$ for the particle velocity, we can write the second-order acoustic wave equation (1) as the following first-order system:

$$\rho \frac{\partial \mathbf{v}}{\partial t} + \nabla p = 0,$$

$$\frac{1}{\kappa} \frac{\partial p}{\partial t} + \nabla \cdot \mathbf{v} = \frac{\partial i_V}{\partial t}. \tag{2}$$

Using the split-field technique (e.g. Chew & Weedon 1994; Collino & Tsogka 2001), we may split the pressure into two parts in a 2-D model, namely $p = p_x + p_y$, then we can further write eq. (2) as

$$\frac{\partial v_x}{\partial t} = -\frac{1}{\rho} \left(\frac{\partial p_x}{\partial x} + \frac{\partial p_y}{\partial x} \right),$$

$$\frac{\partial v_y}{\partial t} = -\frac{1}{\rho} \left(\frac{\partial p_x}{\partial y} + \frac{\partial p_y}{\partial y} \right),$$

$$\frac{\partial p_x}{\partial t} = -\kappa \frac{\partial v_x}{\partial x},$$

$$\frac{\partial p_y}{\partial t} = -\kappa \frac{\partial v_y}{\partial y}, \tag{3}$$

where the source term $\partial i_V/\partial t$ has been ignored for simplicity.

Let $\mathbf{v} = (v_x, v_y)^T$ and $\mathbf{p} = (p_x, p_y)^T$. Then the first-order system (3) can be expressed in a compact form with explicit first-order temporal derivatives:

$$\frac{\partial \mathbf{v}}{\partial t} = \mathbf{A}\mathbf{p},$$

$$\frac{\partial \mathbf{p}}{\partial t} = \mathbf{B}\mathbf{v}, \tag{4}$$

where $\mathbf{A}$ and $\mathbf{B}$ are two matrices formed by spatial derivatives, multiplied by the reciprocal of the density ρ and the elastic coefficient κ, respectively:

$$\mathbf{A} = \begin{bmatrix} -\frac{1}{\rho}\frac{\partial}{\partial x} & -\frac{1}{\rho}\frac{\partial}{\partial x} \\ -\frac{1}{\rho}\frac{\partial}{\partial y} & -\frac{1}{\rho}\frac{\partial}{\partial y} \end{bmatrix}, \qquad \mathbf{B} = \begin{bmatrix} -\kappa\frac{\partial}{\partial x} & 0 \\ 0 & -\kappa\frac{\partial}{\partial y} \end{bmatrix}.$$

The temporal derivatives in eq. (4) can be approximated by the central difference. To do so, we first expand the velocity $\mathbf{v}$ at mid-points $t \pm \Delta t/2$ and pressure $\mathbf{p}$ at grid points $t + \Delta t$ by Taylor series. Then we truncate the expansions up to the fourth order $\mathcal{O}(\Delta t^4)$, and apply eq. (4) and its second- and third-order time derivatives to obtain:

$$\mathbf{v}\left(t + \frac{1}{2}\Delta t\right) - \mathbf{v}\left(t - \frac{1}{2}\Delta t\right) \approx \left(\Delta t \mathbf{A} + \frac{1}{24}\Delta t^3 \mathbf{A}\mathbf{B}\mathbf{A}\right)\mathbf{p}(t),$$

$$\mathbf{p}(t + \Delta t) - \mathbf{p}(t) \approx \left(\Delta t \mathbf{B} + \frac{1}{24}\Delta t^3 \mathbf{B}\mathbf{A}\mathbf{B}\right)\mathbf{v}\left(t + \frac{1}{2}\Delta t\right), \tag{5}$$

which lead to a temporal fourth-order semi-discrete scheme. It reduces to second order (Virieux 1986) when we remove the cubic terms in eq. (5). The remaining spatial derivatives can be discretized with PSM, which we will address in the next section.

3 CENTRED- AND STAGGERED-GRID FOURIER PSEUDOSPECTRAL DERIVATIVES

As in Witte & Richards (1990) and Corrêa *et al.* (2002), we define the first-order Fourier derivative of a function $u(x)$, discretized over a finite grid of N points, by

$$\mathcal{D}_x u(x_i) = \mathcal{DFT}^{-1}\left\{-jk_x \mathcal{DFT}[u(x_i)]\right\}, \tag{6}$$

where $j = \sqrt{-1}$, and $x_i = i\Delta x$, $i = 0, 1, \ldots, N - 1$, with Δx being the sampling interval. The parameter k_x in eq. (6) is the discrete wavenumber, given by $k_x = 2n\pi/(N\Delta x)$ for some integer n. For an even N, we can choose $-N/2 \leq n < N/2$, where $n = -N/2$ corresponds to the Nyquist wavenumber. For an odd N, we can choose $-N/2 < n < N/2$, and in this case the Nyquist wavenumber does not correspond to one of the grid points. The abbreviations $\mathcal{DFT}$ and $\mathcal{DFT}^{-1}$ in eq. (6) denote the forward and inverse discrete Fourier transforms, respectively.

The half-grid-spacing phase-shift of the standard Fourier derivative (6) gives the staggered-grid version of the first-order derivative of $u(x)$ (Witte & Richards 1990):

$$\mathcal{D}_x^{\pm} u\left(x_{i\pm\frac{1}{2}}\right) = \mathcal{DFT}^{-1}\left\{-jk_x \exp\left(\frac{\mp jk_x \Delta x}{2}\right)\mathcal{DFT}[u(x_i)]\right\}, \tag{7}$$

where '$\pm$' denote the forward and backward differentiations. Compared with the conventional Fourier derivative (6), the staggered-grid Fourier pseudospectral differentiation (7) has an advantage of reducing ripple errors caused by phase jumps at the Nyquist wavenumber. A more detailed analysis for the staggered-grid Fourier pseudospectral method can be found in Corrêa *et al.* (2002).

The high-order derivatives at mid-points $x_{i \pm 1/2}$ can be calculated by simply changing the differentiation factor $-jk_x$ to $(-jk_x)^m$ in eq. (7):

$$\mathcal{D}_{x^m}^{\pm} u\left(x_{i\pm\frac{1}{2}}\right) = \mathcal{DFT}^{-1}\left\{(-jk_x)^m \exp\left(\frac{\mp jk_x \Delta x}{2}\right)\mathcal{DFT}[u(x_i)]\right\}, \tag{8}$$

for an odd m. When m is even, the mth derivatives at point x_i should be calculated by recursively using the forward and backward derivative formula (7) alternatively $m/2$ times or simply by using the formula:

$$\mathcal{D}_{x^m} u(x_i) = \mathcal{DFT}^{-1}\{(-jk_x)^m \mathcal{DFT}[u(x_i)]\}. \tag{9}$$

For the spatial discretization, we approximate the spatial derivatives in eq. (5) by appropriate Fourier derivatives defined above and obtain the following fully discrete scheme for the acoustic wave equations (4):

$$v_x^{t+\frac{1}{2}\Delta t} = v_x^{t-\frac{1}{2}\Delta t} - \left[\Delta t b \mathcal{D}_x^+ + \frac{1}{24}\Delta t^3 b^2 \kappa \left(\mathcal{D}_{x^3}^+ + \mathcal{D}_x^+ D_{y^2}\right)\right]\left(p_x^t + p_y^t\right),$$

$$v_y^{t+\frac{1}{2}\Delta t} = v_y^{t-\frac{1}{2}\Delta t} - \left[\Delta t b \mathcal{D}_y^+ + \frac{1}{24}\Delta t^3 b^2 \kappa \left(\mathcal{D}_{x^2}\mathcal{D}_y^+ + \mathcal{D}_{y^3}^+\right)\right]\left(p_x^t + p_y^t\right),$$

$$p_x^{t+\Delta t} = p_x^t - \left[\left(\Delta t \kappa \mathcal{D}_x^- + \frac{1}{24} \Delta t^3 b \kappa^2 \mathcal{D}_{x^3}^- \right) v_x^{t+\frac{1}{2}\Delta t} + \frac{1}{24} \Delta t^3 b \kappa^2 \mathcal{D}_{x^2}^- \mathcal{D}_y^- v_y^{t+\frac{1}{2}\Delta t} \right],$$

$$p_y^{t+\Delta t} = p_y^t - \left[\frac{1}{24} \Delta t^3 b \kappa^2 \mathcal{D}_x^- \mathcal{D}_{y^2}^- v_x^{t+\frac{1}{2}\Delta t} + \left(\Delta t \kappa \mathcal{D}_y^- + \frac{1}{24} \Delta t^3 b \kappa^2 \mathcal{D}_{y^3}^- \right) v_y^{t+\frac{1}{2}\Delta t} \right], \tag{10}$$

where b is the buoyancy, which equals to the reciprocal of the density ρ.

When handling the cubic terms in eq. (10), we have made an assumption that the buoyancy b and bulk module κ do not depend or depend weakly on space. This assumption allows us to move b and κ directly out of each Fourier derivative. It simplifies the numerical scheme at the expense of slightly losing accuracies around the locations where the material properties b and κ vary. Despite the assumption, the scheme is still sufficiently accurate when compared with the acoustic wave equation with constant density, which is frequently used in RTM and waveform inversion (Tarantola 1984; Zhang & Zhang 2009). Moreover, all the coefficients involved in the terms with the first-order spatial differentiation operators preserve most of the variable information on the material properties, so the treatments for those cubic terms do not affect the accuracy of the entire scheme much.

4 DISPERSION RELATION AND STABILITY CONDITION

In this section, we study the stability and dispersion relation of scheme (10). As the major interest of this work is to improve the temporal accuracy and stability, we shall not consider the spatial discretizations involved in scheme (10). Then by summing up the implicit split pressure p_x and p_y we can obtain the following semi-discrete fourth-order scheme:

$$v_x \left(t + \frac{1}{2}\Delta t \right) = v_x \left(t - \frac{1}{2}\Delta t \right) - \left[\Delta t b \frac{\partial}{\partial x} + \frac{1}{24} \Delta t^3 b^2 \kappa \left(\frac{\partial^3}{\partial x^3} + \frac{\partial}{\partial x} \frac{\partial^2}{\partial y^2} \right) \right] p(t),$$

$$v_y \left(t + \frac{1}{2}\Delta t \right) = v_y \left(t - \frac{1}{2}\Delta t \right) - \left[\Delta t b \frac{\partial}{\partial y} + \frac{1}{24} \Delta t^3 b^2 \kappa \left(\frac{\partial^2}{\partial x^2} \frac{\partial}{\partial y} + \frac{\partial^3}{\partial y^3} \right) \right] p(t),$$

$$p(t + \Delta t) = p(t) - \left[\Delta t \kappa \frac{\partial}{\partial x} + \frac{1}{24} \Delta t^3 b \kappa^2 \left(\frac{\partial^3}{\partial x^3} + \frac{\partial}{\partial x} \frac{\partial^2}{\partial y^2} \right) \right] v_x \left(t + \frac{1}{2}\Delta t \right),$$

$$- \left[\Delta t \kappa \frac{\partial}{\partial y} + \frac{1}{24} \Delta t^3 b \kappa^2 \left(\frac{\partial^2}{\partial x^2} \frac{\partial}{\partial y} + \frac{\partial^3}{\partial y^3} \right) \right] v_y \left(t + \frac{1}{2}\Delta t \right). \tag{11}$$

After appropriate manipulations, we can eliminate two components v_x and v_y of the particle velocity and leave only pressure p in eq. (11) to obtain the following semi-discrete acoustic wave equation with temporal fourth-order accuracy:

$$p(t + \Delta t) - 2p(t) + p(t - \Delta t) = \left[\Delta t^2 b \kappa \left(\frac{\partial^2}{\partial x^2} + \frac{\partial^2}{\partial y^2} \right) + \frac{1}{12} \Delta t^4 b^2 \kappa^2 \left(\frac{\partial^2}{\partial x^2} + \frac{\partial^2}{\partial y^2} \right)^2 + \left(\frac{1}{24} \right)^2 \Delta t^6 b^3 \kappa^3 \left(\frac{\partial^2}{\partial x^2} + \frac{\partial^2}{\partial y^2} \right)^3 \right] p(t). \tag{12}$$

Now we can readily derive the dispersion relation of eq. (12) by simply replacing the pressure $p(t)$ by a homogeneous plane wave solution $p(t) = \exp[j(\omega t - k_x x - k_y y)]$:

$$\sin^2 \left(\frac{\omega \Delta t}{2} \right) = \frac{1}{4} \left(k v \Delta t - \frac{1}{24} k^3 v^3 \Delta t^3 \right)^2, \tag{13}$$

where ω is the angular frequency, k_x and k_y are the wavenumbers in x- and y-directions, respectively, $k = \sqrt{k_x^2 + k_y^2}$, and $v = \sqrt{\kappa/\rho}$ is the acoustic velocity. Compared with the dispersion relation of the numerical scheme derived by Chen (2009) for the second-order acoustic wave equation, the relation (13) has an advantage in approximating the true velocity for relatively large wavenumbers.

Let $v' = \omega/k$ be the phase velocity, which is determined by eq. (13). Then the normalized phase velocity can be given by

$$\frac{v'}{v} = \frac{2}{r k \Delta x} \sin^{-1} \left\{ \frac{r k \Delta x}{2} \left[1 - \frac{(r k \Delta x)^2}{24} \right] \right\}, \tag{14}$$

where $r = v \Delta t / \Delta x$ is the CFL condition number.

Fig. 1 shows the normalized phase velocities with different CFL condition numbers. All normalized phase velocities have about the same accuracy that approaches 1.0 in the region of low wavenumbers. However, it is important to observe that the phase velocities still preserve good accuracy for relatively large wavenumbers, especially for $r = 0.3$. For the larger CFL condition number r, the dispersion curves deviate very slowly from the exact value as the wavenumber increases.

Using the condition that $\sin^2(\omega \Delta t/2) \leq 1$, we deduce from eq. (13) the following stability condition for eq. (11):

$$0 \leq k v \Delta t - \frac{1}{24} k^3 v^3 \Delta t^3 \leq 2. \tag{15}$$

Then we obtain the condition by solving the above inequality:
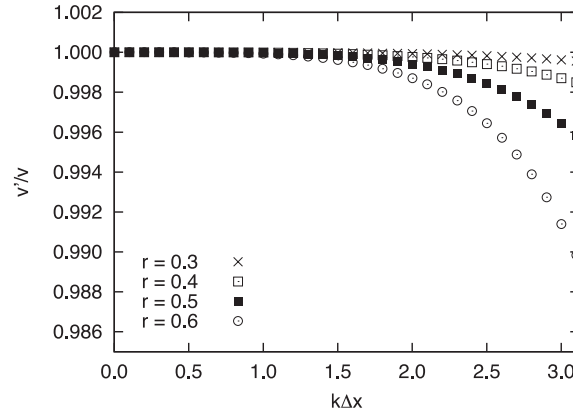
$$k v \Delta t \leq 2\sqrt{6}. \tag{16}$$

Figure 1. Normalized phase velocities with different CFL condition numbers.

For a model with the uniform grid spacing $\Delta x = \Delta y$, we have the Nyquist wavenumbers $k_x = k_y = \pi / \Delta x$. Then using (16), we come to the following explicit stability condition:

$$r = \frac{v \Delta t}{\Delta x} \leq \frac{2\sqrt{3}}{\pi}. \tag{17}$$

This defines a stability region, which is about 2.45 times of that for the second-order PSM, namely $r \leq \sqrt{2}/\pi$, and it is also much larger than that of the fourth-order scheme proposed by Chen (2009). Therefore, we may use larger time steps in numerical simulations with the new scheme when spatial grid sizes are fixed.

5 PML BOUNDARY CONDITIONS

As it is well known, boundary conditions are of great importance to seismic modelling. To accurately simulate seismic waves propagating in an infinite medium, we need to truncate the physical region by means of some damping layers to absorb spurious reflections caused by artificial boundaries. Exponential absorbing boundary conditions have proved to be easy to implement for the first-order acoustic wave equations, but the damping layers must be sufficiently wide to effectively absorb the outgoing waves (e.g. Cerjan *et al.* 1985). On the other hand, the PML boundary conditions are more frequently used and allow narrower damping layers to eliminate spurious reflections. Moreover, the PMLs are very simple and easy to implement for the first-order wave equations.

Following the derivations in Collino & Tsogka (2001), we incorporate the PML boundary conditions in eq. (4) by inserting some terms related to wavefields $\mathbf{p}$, $\mathbf{v}$ and the attenuation matrix $\boldsymbol{\Gamma}$ on the left-hand side of system (4):

$$\frac{\partial \mathbf{v}}{\partial t} + \boldsymbol{\Gamma} \mathbf{v} = \mathbf{A} \mathbf{p},$$

$$\frac{\partial \mathbf{p}}{\partial t} + \boldsymbol{\Gamma} \mathbf{p} = \mathbf{B} \mathbf{v}, \tag{18}$$

where $\boldsymbol{\Gamma}$ is a diagonal matrix with its diagonal entries ξ_x and ξ_y, which are attenuation factors and vanish in the non-PML regions.

If we expand $\mathbf{p}$ and $\mathbf{v}$ in time by Taylor series up to the fourth order, as described in Section 2, we can rewrite eq. (18) as follows:

$$\mathbf{v}\left(t + \frac{1}{2}\Delta t\right) - \mathbf{v}\left(t - \frac{1}{2}\Delta t\right) \approx \left[\Delta t \mathbf{A} + \frac{1}{24}\Delta t^3 (\mathbf{ABA} + \boldsymbol{\Gamma}^2 \mathbf{A} + \mathbf{A}\boldsymbol{\Gamma}^2 + \boldsymbol{\Gamma} \mathbf{A} \boldsymbol{\Gamma})\right] \mathbf{p}(t),$$

$$- \left[\Delta t \boldsymbol{\Gamma} + \frac{1}{24}\Delta t^3 \left(\mathbf{AB}\boldsymbol{\Gamma} + \mathbf{A}\boldsymbol{\Gamma}\mathbf{B} + \boldsymbol{\Gamma}\mathbf{AB} + \boldsymbol{\Gamma}^3\right)\right] \mathbf{v}(t),$$

$$\mathbf{p}(t + \Delta t) - \mathbf{p}(t) \approx \left[\Delta t \mathbf{B} + \frac{1}{24}\Delta t^3 \left(\mathbf{BAB} + \boldsymbol{\Gamma}^2 \mathbf{B} + \mathbf{B}\boldsymbol{\Gamma}^2 + \boldsymbol{\Gamma}\mathbf{B}\boldsymbol{\Gamma}\right)\right] \mathbf{v}\left(t + \frac{1}{2}\Delta t\right),$$

$$- \left[\Delta t \boldsymbol{\Gamma} + \frac{1}{24}\Delta t^3 \left(\mathbf{BA}\boldsymbol{\Gamma} + \mathbf{B}\boldsymbol{\Gamma}\mathbf{A} + \boldsymbol{\Gamma}\mathbf{BA} + \boldsymbol{\Gamma}^3\right)\right] \mathbf{p}\left(t + \frac{1}{2}\Delta t\right). \tag{19}$$

By dropping those cross-terms between $\mathbf{A}$ and $\boldsymbol{\Gamma}$ (resp. $\mathbf{B}$ and $\boldsymbol{\Gamma}$) in eq. (19), then moving those terms involving $\boldsymbol{\Gamma}$ to the left-hand side, we obtain:

$$\mathbf{v}\left(t + \frac{1}{2}\Delta t\right) - \mathbf{v}\left(t - \frac{1}{2}\Delta t\right) + \left(\Delta t \boldsymbol{\Gamma} + \frac{1}{24}\Delta t^3 \boldsymbol{\Gamma}^3\right) \mathbf{v}(t) \approx \left(\Delta t \mathbf{A} + \frac{1}{24}\Delta t^3 \mathbf{ABA}\right) \mathbf{p}(t),$$

$$\mathbf{p}(t + \Delta t) - \mathbf{p}(t) + \left(\Delta t \boldsymbol{\Gamma} + \frac{1}{24}\Delta t^3 \boldsymbol{\Gamma}^3\right) \mathbf{p}\left(t + \frac{1}{2}\Delta t\right) \approx \left(\Delta t \mathbf{B} + \frac{1}{24}\Delta t^3 \mathbf{BAB}\right) \mathbf{v}\left(t + \frac{1}{2}\Delta t\right). \tag{20}$$

These approximations are reasonable since the elements of $\mathbf{\Gamma}$ vanish in the computational domain, and it does not have much effect on the temporal accuracy by dropping the cross-terms.

Now we approximate $\mathbf{v}(t)$ by the average of its values at $t - \Delta t/2$ and $t + \Delta t/2$, and $\mathbf{p}(t + \Delta t/2)$ by the average of its values at t and $t + \Delta t$ in eq. (20) to derive the fully discrete scheme with the staggered-grid Fourier derivatives:

$$v_x^{t+\frac{1}{2}\Delta t} = \alpha_x v_x^{t-\frac{1}{2}\Delta t} - \beta_x \left[\Delta t b \mathcal{D}_x^+ + \frac{1}{24}\Delta t^3 b^2 \kappa \left(\mathcal{D}_{x^3}^+ + \mathcal{D}_x^+ \mathcal{D}_{y^2} \right) \right] \left(p_x^t + p_y^t \right),$$

$$v_y^{t+\frac{1}{2}\Delta t} = \alpha_y v_y^{t-\frac{1}{2}\Delta t} - \beta_y \left[\Delta t b \mathcal{D}_y^+ + \frac{1}{24}\Delta t^3 b^2 \kappa \left(\mathcal{D}_{x^2}\mathcal{D}_y^+ + \mathcal{D}_{y^3}^+ \right) \right] \left(p_x^t + p_y^t \right),$$

$$p_x^{t+\Delta t} = \alpha_x p_x^t - \beta_x \left[\left(\Delta t \kappa \mathcal{D}_x^- + \frac{1}{24}\Delta t^3 b \kappa^2 \mathcal{D}_{x^3}^- \right) v_x^{t+\frac{1}{2}\Delta t} + \frac{1}{24}\Delta t^3 b \kappa^2 \mathcal{D}_{x^2}\mathcal{D}_y^- v_y^{t+\frac{1}{2}\Delta t} \right],$$

$$p_y^{t+\Delta t} = \alpha_y p_y^t - \beta_y \left[\frac{1}{24}\Delta t^3 b \kappa^2 \mathcal{D}_x^- \mathcal{D}_{y^2} v_x^{t+\frac{1}{2}\Delta t} + \left(\Delta t \kappa \mathcal{D}_y^- + \frac{1}{24}\Delta t^3 b \kappa^2 \mathcal{D}_{y^3}^- \right) v_y^{t+\frac{1}{2}\Delta t} \right], \qquad (21)$$

where α_i and β_i $(i = x, y)$ are given by

$$\alpha_i = \frac{1 - \frac{1}{2}\Delta t \xi_i - \frac{1}{48}\Delta t^3 \xi_i^3}{1 + \frac{1}{2}\Delta t \xi_i + \frac{1}{48}\Delta t^3 \xi_i^3}, \qquad \beta_i = \frac{1}{1 + \frac{1}{2}\Delta t \xi_i + \frac{1}{48}\Delta t^3 \xi_i^3}.$$

When ξ_x and ξ_y are chosen to be 0 in the PML regions, that is, $\alpha_i = \beta_i = 1$, the fully discrete scheme (21) with PML boundary conditions reduces to scheme (10).

6 NUMERICAL EXPERIMENTS

6.1 Accuracy and convergence

In this section, we present some numerical examples to verify the accuracy of the new scheme (21) for solving the first-order acoustic wave equations (2). For this, we consider a bilayered medium with constant density and two different velocities, which are called model 1 and model 2 below for convenience. The velocity of the first layer is set to be $3000\,\mathrm{m\,s^{-1}}$, while the velocities of the second layer are set to be $4000\,\mathrm{m\,s^{-1}}$ and $6000\,\mathrm{m\,s^{-1}}$ for models 1 and 2, respectively, where the latter case gives a larger velocity contrast. The computational grid is 256×256, with the grid spacings $\Delta x = \Delta y = 10$ m for both models. We use a Gaussian wavelet source $s(t) = (t - t_0) \exp[-\pi^2 f_0^2 (t - t_0)^2]$ in our simulations with central frequency $f_0 = 20$ Hz and time delay $t_0 = 1.5\sqrt{6}/(\pi f_0)$. To ensure that the evaluated phase velocity approximates the true velocity for large wavenumbers, we choose a reasonable time step $\Delta t = 0.001$s. Configurations of the source and receivers can be seen in Fig. 2. The source is located in the upper layer with a distance of $500\,\mathrm{m}$ to the interface. Two receivers are placed in the upper and lower layers: the one in the upper layer is about $500\,\mathrm{m}$ away from the source in the horizontal direction; and the other in the lower layer has the same abscissa as the first one but is $500\,\mathrm{m}$ below the interface.

Waveforms at two receivers in two different models are shown in Fig. 3, where the analytic solutions computed using the program codes by Diaz & Ezziani (2010) are plotted for comparisons. One may observe from these figures that the numerical solution matches well with the analytic solution, even at the peaks of the reflection and transmission events. We have used the parameter averaging technique developed by Moczo *et al.* (2002) to treat the discontinuity across the interface in the simulations, and seen that enlarging the velocity contrast across the medium interface does not cause more numerical errors: the maximum relative errors are respectively 0.58 per cent and 0.13 per cent at
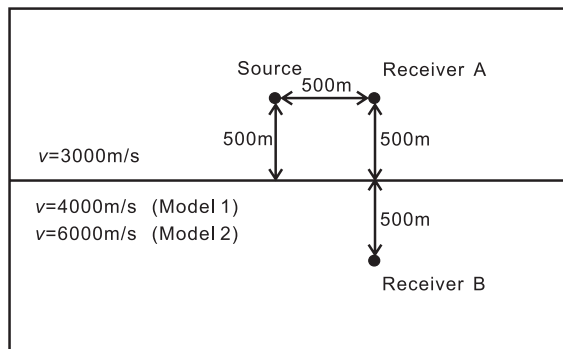

Figure 2. Bilayered medium for models 1 and 2 with source and receiver configuration. The source is located in the upper layer with a distance of $500\,\mathrm{m}$ to the interface. Two receivers are placed, respectively, in the upper and lower layers, with one being $500\,\mathrm{m}$ away from the source in the horizontal direction and the other in the lower layer having the same abscissa as the first one but $500\,\mathrm{m}$ below the interface.
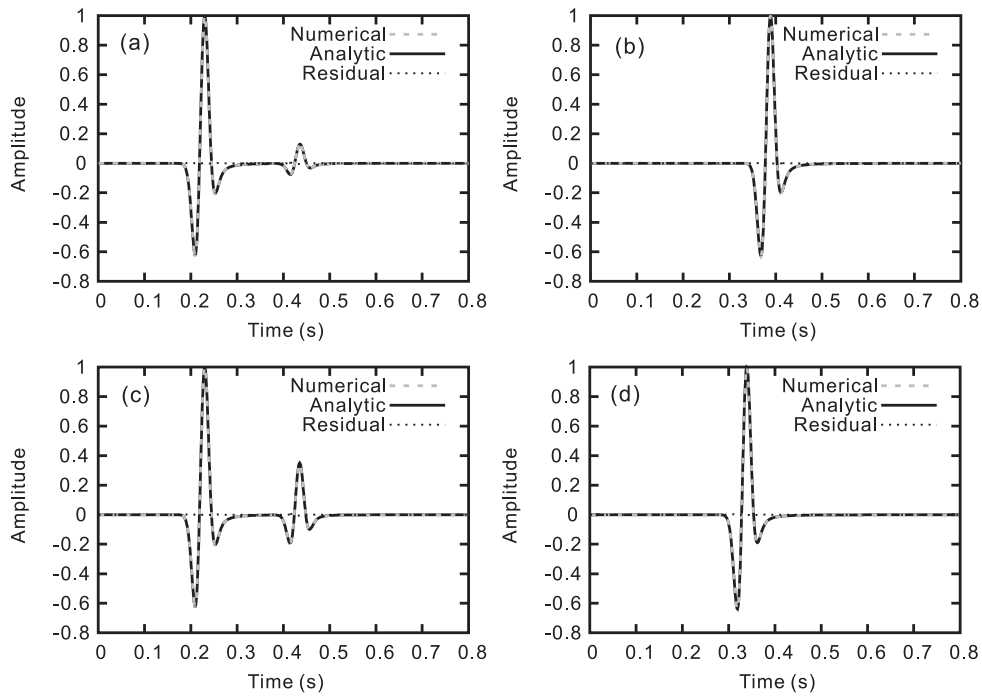
Figure 3. Comparisons of the waveforms at receivers A and B, computed by both the temporal fourth-order scheme and the analytic method (Diaz & Ezziani 2010). The graphs (a) and (b) are computed for model 1 with the velocities of 3000 and 4000 m s^{-1}, respectively, in the first and second layers; the graphs (c) and (d) are for model 2 with the velocities of 3000 and 6000 m s^{-1}, respectively, for the two layers. Waveforms are all normalized by their individual maximum amplitudes.

points A and B for model 1, while the maximum relative error is still 0.58 per cent at point A, but increases only slightly at point B, about 0.1 per cent more, for model 2.

To better quantify the differences between two waveforms in Fig. 3 that we compared, we now use the locally normalized time-frequency (TF) envelope and phase misfit criteria (Kristeková *et al.* 2006, 2009), denoted respectively by TFEM and TFPM:

$$\mathrm{TFEM}(t, f) = \frac{\Delta A(t, f)}{A_r(t, f)},$$

$$\mathrm{TFPM}(t, f) = \frac{\Delta \phi(t, f)}{\pi}, \tag{22}$$

where $A(t, f)$ and $\phi(t, f)$ are the envelope and phase of a signal, given by $A(t, f) = |W(t, f)|$ and $\phi(t, f) = \mathrm{Arg}[W(t, f)]$. Here $W(t, f)$ can be calculated by wavelet transforms (Kristeková *et al.* 2006, 2009). The subscript '*r*' indicates a reference signal, that is, the analytic solution involved in seismic modelling.

Fig. 4 shows the TF envelope and phase misfits between the computed and analytic solutions at points A and B in models 1 and 2. We can see that the distribution of nonzero values of TFEM(*t, f*) in the (*t, f*) plane corresponds to the differences of two waveforms, and the differences are so small that we can not distinguish the two. However, we can easily recognize from the figure the locations where the envelope of the computed waveform is large or small when compared with that of the analytic solution. The misfits distribute basically around the peaks of the direct and reflected waves. The stronger the heterogeneity is, the larger the misfits are; see Figs 4(a)–(b) and Figs 4(e)–(f). The phase misfits TFPM(*t, f*) tell the locations where the phase of the computed waveform is advanced or delayed. Figs 4(d) and (h) clearly show the phases are advanced when compared with the analytic solutions in model 2. On the other hand, model 1 has a smaller velocity contrast, and the misfits are hard to identify; see Figs 4(c) and (g).

To measure the convergence of the proposed fourth-order scheme quantitatively, we use the following root mean square (rms) deviation E of the numerical solution p from the analytic solution p_0 (De Hoop 1960):

$$E = \|p - p_0\|_{L^2} \approx \left\{ \frac{1}{N_x N_y} \sum_{i=1}^{N_x} \sum_{j=1}^{N_y} \left[p(x_i, y_i, t_k) - p_0(x_j, y_j, t_k) \right]^2 \right\}^{\frac{1}{2}}, \tag{23}$$

where $p(x_i, y_j, t_k)$ is the wavefield at grid point (x_i, y_j) and time t_k.

We use three different time steps, that is, $\Delta t = 0.0005$, 0.001 and 0.002 s, to simulate the wavefields in the bilayered model 1. The number of grid points is taken to be 472×472, but with extra 20 grid points extended in both *x*- and *y*-directions as the PML boundary layer. In the rms deviation error measurement (23), we select $N_x \times N_y = 201 \times 201$ grid points around the centre of the model, and take the Gaussian wavelet source located at (2360 m, 1860 m) in our simulation. The maximum time for the wavefield propagation is 0.6 s. Fig. 5 shows the
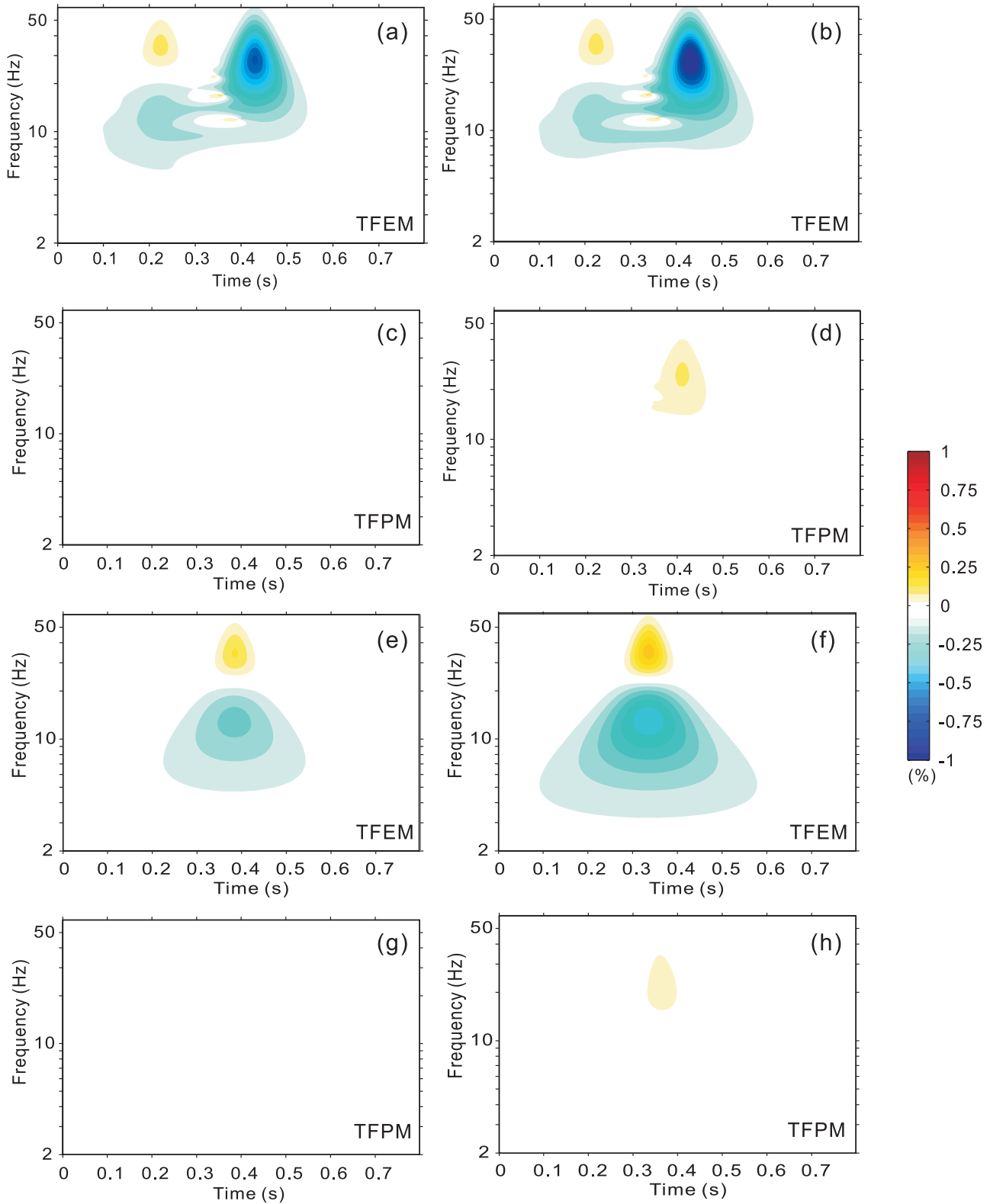
Figure 4. Locally normalized TFEM and TFPM misfits between computed and analytic solutions. The TF representations on the top panel with graphs (a)–(d) are computed for waveforms at receiver A; the graphs (e)–(h) on the bottom panel are computed for receiver B. The left panel with TFEM and TFPM misfits is for model 1; the right panel is for model 2.
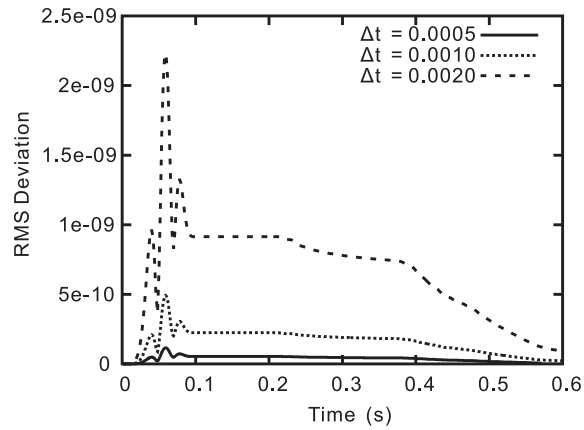
Figure 5. The rms deviation errors of the numerical solutions from the analytic solutions computed with three different time steps.

numerical errors computed with three different time steps. We can observe from this figure that the errors decrease as Δt, which confirms clearly the convergence of the proposed scheme.

6.2 Stability and computational costs

In this section, we deliberately design a heterogeneous model containing a salt dome (see Fig. 6) to test the stability of the new fourth-order scheme. The velocity of the model ranges from 2500 m s^{-1} in the top layer to 6500 m s^{-1} in the bottom layer. The salt dome is upsurging from the bottom and going up to the second layer, with its property slightly assimilated with surrounding media. The model size is selected to be 11775 m × 5375 m and discretized by the cells of equal size 25 m × 25 m. For the sake of convenience in marking events on common shot gathers (CSGs), we denote by the notations L_i the interfaces between layers; see Fig. 6.

Fig. 7 shows snapshots of the wavefield at various times calculated with different time steps. As in the previous simulations, a Gaussian wavelet is used here, but with a peak frequency of 25 Hz, which meets the requirement of at least 2 grid points per wavelength for the PSM in the low velocity layer. By calculations, we find the maximum time step for stability is 0.0042 s. So we choose a slightly smaller time step 0.0038 s, considering both the stability and the fact that the impact of the PML terms that were dropped in eq. (21) may not be negligible at the bottom layer with the largest velocity. The result is shown in Fig. 7(a). In addition, we test the numerical effect with the maximum time step 0.0042 s, and the result is presented in Fig. 7(b), from which we can see that the scheme becomes unstable at the bottom layer.

In these simulations, 20 grid points were added to the four sides of the model to absorb spurious reflections. Indeed, one can observe the superior boundary attenuation near the bottom boundary, as shown in Fig. 7(a). The cross-terms dropped in eq. (10) seem to have little effect on the final numerical solution.

In Table 1, we have also provided a comparison of the computational costs between the standard second-order scheme and the new fourth-order scheme with different time steps. Only three FFTs and four inverse fast Fourier transforms (IFFTs) are needed at each time step for the second-order scheme, whereas three FFTs and ten IFFTs are required for the fourth-order scheme. We can see that the computational time required by the second-order scheme is 29.37s, which is 1.83 times faster than that of the fourth-order scheme when computed with the same time step $\Delta t = 0.001$ s, approximating the theoretical speedup 1.86. The same has been observed when the fourth-order scheme is used with different time steps, especially the scheme with $\Delta t = 0.0025$ s is 1.35 times faster than the second-order scheme with $\Delta t = 0.001$ s. However, we have not compared the second-order scheme with the fourth-order one for larger time steps, since the stability condition is violated for the second-order scheme when the time step $\Delta t = 0.0025$ s is used. This indicates that the new fourth-order scheme can achieve better accuracy without losing its efficiency.
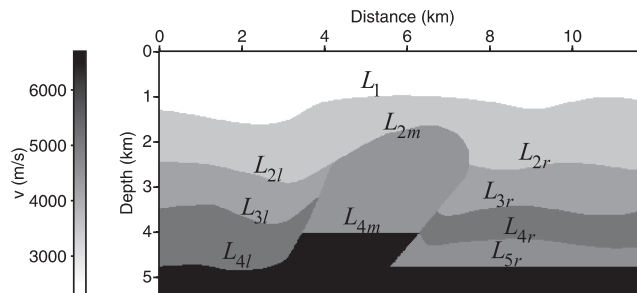

Figure 6. Layered heterogenous media with a salt dome upsurging to the second layer. On the left side of the salt is a five-layer structure whose velocities are increasing with depth; and on the right is a six-layer structure with a low velocity medium lying above the bottom layer.
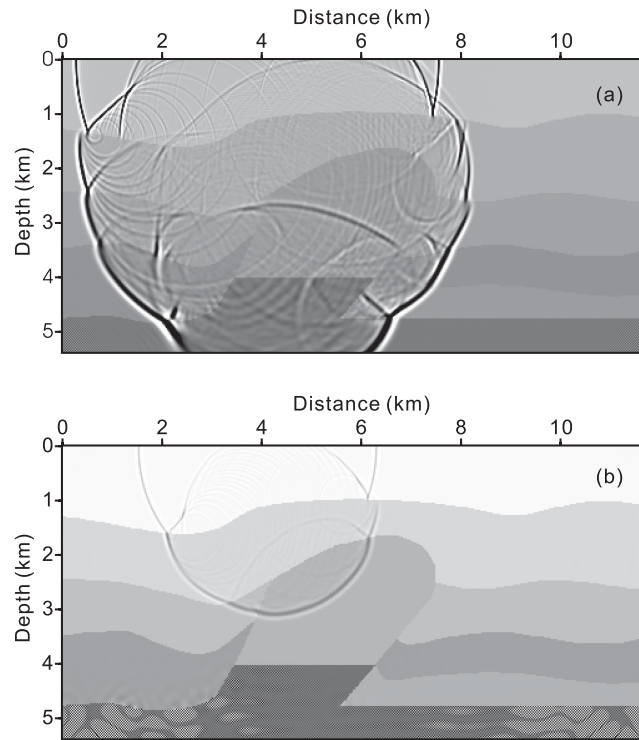
Figure 7. Snapshot of the wavefields at 1.5 s in panel (a) with $\Delta t = 0.0038$ s and at 1.0 s in panel (b) with $\Delta t = 0.0042$ s, overlaid by the velocity model on the background. The source is a Gaussian wavelet located at (3925 m, 50 m) with peak frequency 25 Hz.

Table 1. Computational costs of the standard second-order and new temporal fourth-order schemes on a mesh of 512×256 with a total time iteration of 600 steps.

Order (Δt)	2nd (0.001 s)	4th (0.001 s)	4th (0.0025 s)
Transforms	$3FFT + 4IFFT$	$3FFT + 10IFFT$	$3FFT + 10IFFT$
Memory	$6N_xN_y$	$6N_xN_y$	$6N_xN_y$
Time	29.37 s	53.65 s	21.49 s

Finally, we like to make a comparison between the memories of the classical second-order scheme and the new fourth-order scheme. We recall that N_x and N_y are the numbers of grid points in the *x*- and *y*-directions, respectively. It is easy to see that the fourth-order scheme needs a storage of $6N_xN_y$ for the wavefields and their Fourier derivatives, the same as the second-order scheme: four are used to store the wavefields and the other two to store one wavefield's Fourier transform and its corresponding spatial derivative. In comparisons, it requires only a storage of $3N_xN_y$ to compute wavefields directly from the second-order wave equation when an optimized memory configuration is applied. However, it is technically much more difficult for spatial discretizations when PML is used, since the original second-order equation becomes a coupled system of three differential equations with auxiliary variables (Grote & Sim 2010).

6.3 Common shot gathers and reverse time migration

Sufficiently accurate waveform data pre-generated by numerical modelling is of great importance for acquisition configuration and RTM. A well-configured array can maximize the valid signals received for a specific event reflected from a geological structure. In Figs 8(a) and (b) we have shown two CSGs generated by our new scheme with the Ricker wavelet source $s(t) = [1 - 2\pi^2 f_0^2(t - t_0)^2]\exp[-\pi^2 f_0^2(t - t_0)^2]$ located at (0 m, 50 m) and (4925 m, 50 m), respectively, where the parameters f_0 and t_0 are set to be 15 Hz and 0.078 s. From these figures, we can see clear reflection and transmission waves which are perpendicular to the curved interfaces. Compared with other reflections, the one reflected by L_{4m} has a relatively larger amplitude because of the high impedance contrast between the two media across the interface. The reflections and multiples coupled with direct waves at long offsets interacting with each other make events in this area difficult to recognize, see the events at 3.0 s and the offset 6 km in Fig. 8(a). We observe from Fig. 8(a) that all the physically interesting events, such as L_{4r}, L_{5r} and their intersections with the salt, are not well separated, except the event L_{4m} that can be clearly identified. By moving the source by 3925 m away from its first shot location to the centre one can separate those overlaid events in Fig. 8(a); see Fig. 8(b). Because of the shielding effect of the salt dome, it is hard for receivers on the surface to detect the waveforms reflected by the subsalt structures. By increasing offsets along the dip direction, one can extract more detailed geological information, which is significant to geophysical exploration.
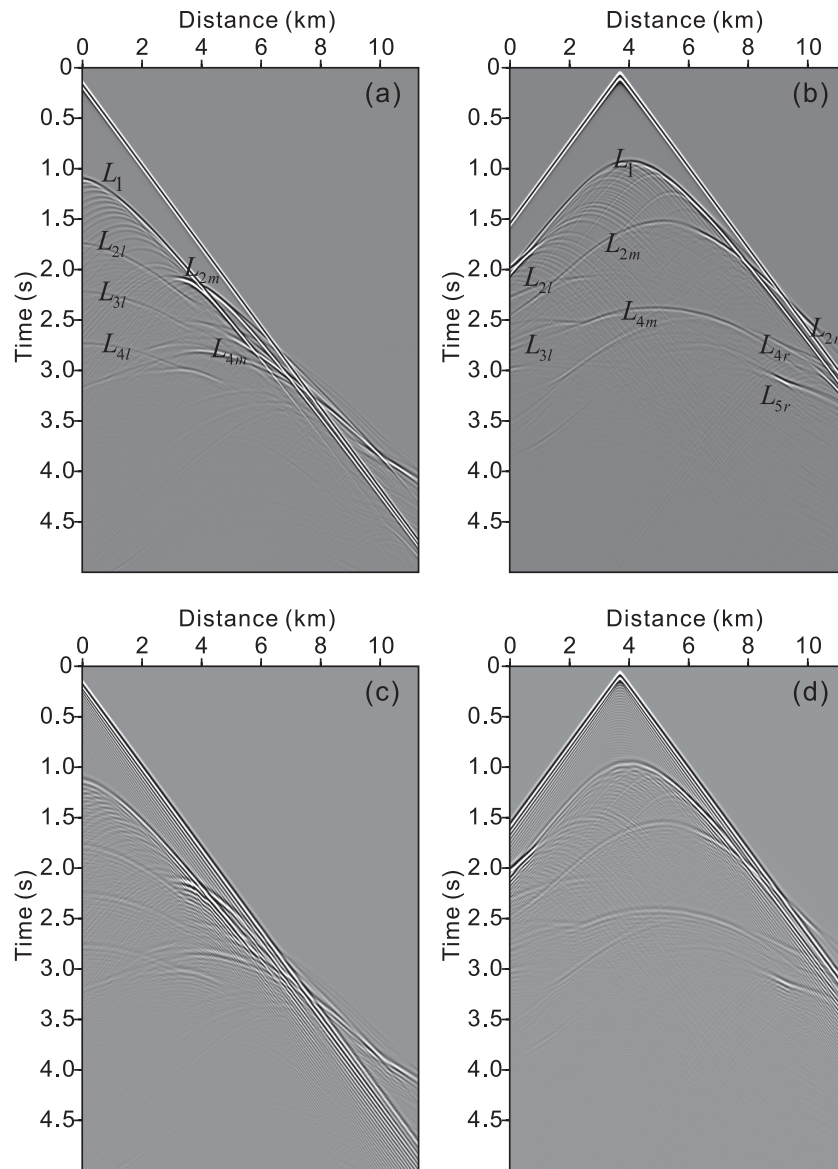
Figure 8. Common shot gathers generated with a Ricker wavelet source of 15 Hz located at points (0 m, 50 m) and (3925 m, 50 m), respectively. Profiles (a) and (b) are computed by the new scheme, while profiles (c) and (d) are computed by the temporal second-order scheme and fourth-order spatial staggered-grid FDM. Events reflected by different interfaces are labelled with L_i on the profiles (a) and (b), where the subscript i in L_i indicates the ith interface, and l, m and r represent events reflected by the interfaces on the left, middle and right of the model individually.

Next, we compare the previous results obtained by the new method with the ones computed by the spatial fourth-order staggered-grid FDM. The synthetic seismograms generated by the FDM are shown in Figs 8(c) and (d). Clearly, numerical dispersion can be seen near the direct waves and the reflected waves, because there are only 3.3 points per wavelength for the FDM in the first layer of the media. However, this is enough for the staggered-grid Fourier PSM. Excessive dispersion may distort the multiples reflected within the layers, which are important for subsalt imaging.

The CSG data generated by the new temporal fourth-order scheme in Section 5 with the shot spacing of 50 m, the receiver spacing of 25 m and the maximum offset of 11 775 m, are applied next for a RTM. The migrated result is shown in Fig. 9, from which we can see that the new scheme handles the complex velocity structure well and provides satisfactory delineations at the salt boundaries, especially for the steeply dipping salt flanks and the overturned salt edges. The step-like layered interfaces which are caused by using straight lines to approximate the curved interfaces are also imaged well.

The RTM with $\Delta t = 0.001$ s is also implemented. Before migration, we refine the CSGs with spline interpolation. By backpropagating the wavefields and convolving them with the interpolated wavefields, we finally obtain the migrated results, which are omitted here as it is very similar to that in Fig. 9. On a cluster of four nodes, the new fourth-order scheme saves about 2.5 hr compared to the second-order scheme which takes about 10 hr.
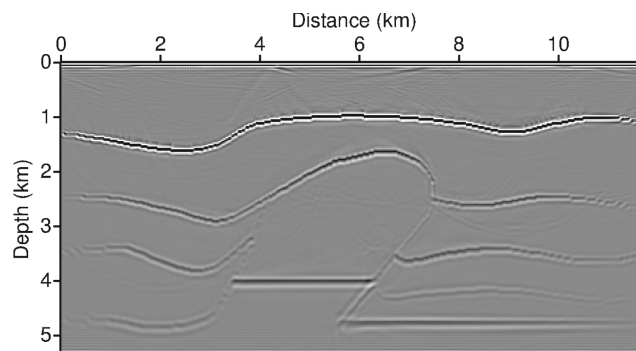
Figure 9. The reverse time migration image of the salt dome model with temporal fourth-order scheme.

7 CONCLUSIONS

In this work, we have proposed a temporal fourth-order scheme for solving the first-order acoustic wave equations in 2-D media. The new scheme relaxes the stability condition and allows a larger time step, and is more efficient and accurate than the classical second-order scheme. To absorb the spurious reflections caused by the artificial boundaries, we incorporate the PML in the first-order equations. The PML attenuates the outgoing waves exponentially and reduces the folding effect of the Fourier transforms used for computing spatial derivatives essentially.

Numerical results for a bilayered model have shown the accuracy and convergence of the new fourth-order scheme. Compared with the standard second-order scheme, the proposed method has a larger stability region and requires less computational efforts when larger time steps are used. The wavefield modelling in heterogeneous media has also demonstrated the flexibility and robustness of the new scheme to handle complex media. The cross-terms that have been dropped in the derivation of the temporal scheme for the PML equations cause little effect on the final numerical accuracy of the scheme. Analyses on snapshots and seismograms at different source locations indicate that accurate wavefields generated by the new scheme can be used to guide the configuration of acquisition. Experiments for RTM have also demonstrated the efficiency and accuracy of the proposed scheme.

The proposed method can be naturally extended to three dimensions, by simply replacing the 2-D discrete Fourier transform by the 3-D one. The new method can also be accelerated. For instance, for the acceleration of modelling and the RTM, we can implement the algorithm on clusters or port the serial CPU codes to GPU or many-core architectures by simply replacing the FFTs by their counterparts.

REFERENCES

Berenger, J., 1994. A perfectly matched layer for the absorption of electro-magnetic waves, *J. Comput. Phys.,* **114**(2), 185–200.

Cerjan, C., Kosloff, D., Kosloff, R. & Reshef, M., 1985. A nonreflecting boundary condition for discrete acoustic and elastic wave equations, *Geophysics,* **50**(4), 705–708.

Chaljub, E., Komatitsch, D., Vilotte, J.-P., Capdeville, Y., Valette, B. & Festa, G., 2007. Spectral element analysis in seismology, *Geophysics,* **50**(4), 705–708.

Chen, J.B., 2007. High-order time discretizations in seismic modeling, *Geophysics,* **72**(5), SM115–SM122.

Chen, J.B., 2009. Lax-Wendroff and Nyström methods for seismic modelling, *Geophys. Prospect.,* **57**(6), 931–941.

Chew, W.C. & Liu, Q.H., 1996. Perfectly matched layers for elastodynamics: a new absorbing boundary condition, *J. Comput. Acoust.,* **4**, 341–359.

Chew, W.C. & Weedon, W.H., 1994. A 3-D perfectly matched medium from modified Maxwell's equations with stretched coordinates, *Microwave Opt. Tech. Lett.,* **7**, 599–604.

Ciarlet, P.G., 1991. Basic error estimates for elliptic problems, in *Handbook of Numerical Analysis, Vol. II: Finite Element Methods (Part I),* pp. 17–351, eds Ciarlet, P.G. & Lions, J.-L., North-Holland, Amsterdam.

Collino, F. & Tsogka, C., 2001. Application of the PML absorbing layer model to the linear elastodynamic problem in anisotropic heterogeneous media, *Geophysics,* **66**(1), 294–307.

Corrêa, G., Spiegelman, M., Carbotte, S. & Mutter, J., 2002. Centered and staggered Fourier derivatives and Hilbert transforms, *Geophysics,* **67**(5), 1558–1563.

Dablain, M., 1986. The application of high-order differencing to the scalar wave equation, *Geophysics,* **51**(1), 54–66.

De Hoop, A., 1960. A modification of Cagniard's method for solving seismic pulse problems, *Appl. Sci. Res.,* **8**(1), 349–356.

Diaz, J. & Ezziani, A., 2010, Analytical solution for wave propagation in stratified poroelastic medium. Part I: the 2D case, *Comm. Comput. Phys.,* **7**, 171–174.

Drossaert, F. & Giannopoulos, A., 2007. A nonsplit complex frequency-shifted PML based on recursive integration for FDTD modeling of elastic waves, *Geophysics,* **72**(2), T9–T17.

Dumbser, M., Káser, M. & Toro, E., 2007. An arbitrary high order discontinuous Galerkin method for elastic waves on unstructured meshes V: local time stepping and *p*-adaptivity, *Geophys. J. Int.,* **171**, 695–717.

Fornberg, B., 1988. The pseudospectral method: accurate representation of interfaces in elastic wave calculations, *Geophysics,* **53**(5), 625–637.

Gazdag, J., 1981. Modeling of the acoustic wave equation with transform methods, *Geophysics,* **46**(6), 854–859.

Galis, M., Moczo, P. & Kristek, J., 2008. A 3-D hybrid finite-difference–finite-element viscoelastic modelling of seismic wave motion, *Geophys. J. Int.,* **175**(1), 153–184.

Geller, R.J. & Takeuchi, N., 1998. Optimally accurate second-order time-domain finite difference scheme for the elastic equation of motion: one dimensional case, *Geophys. J. Int.,* **135**(1), 48–62.

Grote, M. & Sim, I., 2010. Efficient PML for the wave equation, arXiv. Available at: http://arxiv.org/pdf/1001.0319v1.pdf.

Holberg, O., 1987. Computational aspects of the choice of operator and sampling interval for numerical differentiation in large-scale simulation of wave phenomena *Geophys. Prospect.,* **35**(6), 629–655.

Igel, H., Mora, P. & Riollet, B., 1995. Anisotropic wave propagation through finite-difference grids, *Geophysics,* **60**(4), 1203–1216.

Käser, M. & Dumbser, M., 2006. An arbitrary high order discontinuous Galerkin method for elastic waves on unstructured meshes I: the two-dimensional isotropic case with external source terms, *Geophys. J. Int.,* **166**(2), 855–877.

Käser, M. & de la Puente, J., 2008. Quantitative accuracy analysis of the discontinuous Galerkin method for seismic wave propagation, *Geophys. J. Int.,* **173**(3), 990–999.

Komatitsch, D. & Martin, R., 2007. An unsplit convolutional perfectly matched layer improved at grazing incidence for the seismic wave equation, *Geophysics,* **72**(5), SM155–SM167.

Komatitsch, D. & Tromp, J., 2002. Spectral-element simulation of global seismic wave propagation-I. Validation, *Geophys. J. Int.,* **149**(2), 390–412.

Komatitsch, D. & Tromp, J., 2003. A perfectly matched layer absorbing boundary condition for the second-order seismic wave equation, *Geophys. J. Int.,* **54**(1), 146–153.

Komatitsch, D. & Vilotte, J.P., 1998. The spectral element method: an efficient tool to simulate the seismic response of 2D and 3D geological structures, *Bull. seism. Soc. Am.,* **88**(2), 368–392.

Kosloff, D. & Baysal, E., 1982. Forward modelling by a Fourier method, *Geophysics,* **47**(10), 1402–1412.

Kosloff, D., Filho, A.Q., Tessmer, E. & Behle, A., 1989. Numerical solution of the acoustic and elastic wave equations by a new rapid expansion method, *Geophys. Prospect.,* **37**(4), 383–394.

Kristek, J., Moczo, P. & Galis, M., 2009. A brief summary of some PML formulations and discretizations for the velocity-stress equation of seismic motion, *Studia. Geophys. Geod.,* **53**, 459–474.

Kristeková, M., Kristek, J., Moczo, P. & Day, S.M., 2006. Misfit criteria for quantitative comparison of seismograms, *Bull. seism. Soc. Am.,* **96**, 1836–1850.

Kristeková, M., Kristek, J. & Moczo, P., 2009. Time-frequency misfit and goodness-of-fit criteria for quantitative comparison of time signals, *Geophys. J. Int.,* **178**, 813–825.

Levander, A.R., 1988. Fourth-order finite-difference *P-SV* seismograms, *Geophysics,* **53**(11), 1425–1436.

Liu, Y. & Sen, M.K., 2009a. 2D acoustic wave equation modeling with a new high-accuracy time-space domain finite-difference stencil, in *Proceedings of the 71st EAGE Conference,* Expanded Abstracts, S011, Amsterdam, Netherlands.

Liu, Y. & Sen, M.K., 2009b. Advanced finite-difference methods for seismic modeling, *Geohorizons,* **14**(2), 5–16.

Moczo, P., Kristek, J. & Halada, L., 2000. 3D fourth-order staggered-grid finite-difference schemes: stability and grid dispersion, *Bull. seism. Soc. Am.,* **90**(3), 587–603.

Moczo, P., Kristek, J., Vavrycuk, V, Archuleta, R.J. & Halada, L., 2002. 3D heterogeneous staggered-grid finite-difference modeling of seismic motion with volume harmonic and arithmetic averaging of elastic moduli and densities, *Bull. seism. Soc. Am.,* **92**(8), 3042–3066.

Moczo, P., Kristek, J., Galis, M. & Pazak, P., 2007a. The finite-difference and finite-element modeling of seismic wave propagation and earthquake motion, *Acta Phys. Slovaca,* **57**(2), 177–406.

Moczo, P., Robertsson, J.O.A. & Eisner, L., 2007b. The finite-difference time-domain method for modeling of seismic wave propagation, *Acta Phys. Slovaca,* **57**, 177–406.

Moczo, P., Kristek, J., Galis, M., Chaljub, E. & Etienne, V., 2011. 3-D finite-difference, finite-element, discontinuous-Galerkin and spectral-element schemes analysed for their accuracy with respect to P-wave to S-wave speed ratio, *Geophys. J. Int.,* **187**, 1645–1667.

Pestana, R. & Stoffa, P., 2010. Time evolution of the wave equation using rapid expansion method, *Geophysics,* **75**(4), T121–T131.

Sacks, Z., Kingsland, D., Lee, R. & Lee, J.F., 1995. A perfectly matched anisotropic absorber for use as an absorbing boundary condition, *IEEE Trans. Antennas Propag.,* **43**(12), 1460–1463.

Soubaras, R., 1996. Explicit 3-D migration using equiripple polynomial expansion and Laplacian synthesis, *Geophysics,* **61**(5), 1386–1393.

Soubaras, R. & Zhang, Y., 2008. Two-step explicit marching method for reverse time migration, in *Proceedings of the 78th Annual International Meeting,* SEG, Expanded Abstracts, Vol. **27,** pp. 2272–2276.

Takenaka, H., Wang, Y.B. & Furumura, T., 1999. An efficient approach of the pseudospectral method for modelling of geometrically symmetric seismic wavefield, *Earth Planets Space,* **51**(2), 73–79.

Tal-Ezer, H., Kosloff, D. & Koren, Z., 1987. An accurate scheme for forward seismic modeling, *Geophys. Prospect.,* **35**(5), 479–490.

Tarantola, A., 1984. Inversion of seismic reflection data in the acoustic approximation, *Geophysics,* **49**(8), 1259–1266.

Tessmer, E., 2000. Seismic finite-difference modeling with spatially varying time steps, *Geophysics,* **65**(4), 1290–1293.

Virieux, J., 1986. P-SV wave propagation in heterogeneous media: velocity stress finite-difference method, *Geophysics,* **51**(4), 889–901.

Witte, D. & Richards, P., 1990. The pseudospectral method for simulating wave propagation, in *Computational Acoustics,* pp. 1–18, Vol. 3, eds, Lee, D., Cakmak, A. & Vicknevetsky, R., Elevier Science Publication, North-Holland.

Yang, D.H., Teng, J.W., Zhang, Z.J. & Liu, E., 2003. A nearly analytic discrete method for acoustic and elastic wave equations in anisotropic media, *Bull. seism. Soc. Am.,* **93**(2), 2389–2401.

Yoshimura, Ch., Bielak, J., Hisada, T. & Fernández, A., 2003. Domain reduction method for three-dimensional earthquake modeling in localized regions, Part II: verification and applications, *Bull. seism. Soc. Am.,* **93**, 825–840.

Zhang, Y. & Zhang, G., 2009. One-step extrapolation method for reverse time migration, *Geophysics,* **74**(4), A29–A33.